

Significant change in the electronic behavior associated with structural distortions in the single crystalline SrAg_4As_2

Bing Shen,¹ Eve Emmanouilidou,¹ Xiaoyu Deng,² Alix McCollam,³
Jie Xing,¹ Gabriel Kotliar,² Amalia I. Coldea,⁴ and Ni Ni^{1,*}

¹*Department of Physics and Astronomy and California NanoSystems Institute,
University of California, Los Angeles, CA 90095, USA*

²*Department of Physics and Astronomy, Rutgers University, Piscataway, NJ 08854, USA*

³*High Field Magnet Laboratory (HFML-EMFL), Radboud University, 6525 ED Nijmegen, The Netherlands*

⁴*Clarendon Laboratory, Department of Physics, University of Oxford, Parks Road, Oxford OX1 3PU, UK*
(Dated: December 14, 2024)

Here we report a combined study of transport and thermodynamic measurements on the layered pnictide material SrAg_4As_2 . Upon cooling, a drop in electrical and Hall resistivity, a jump in heat capacity and an increase in susceptibility and magnetoresistance (MR) are observed around 110 K. All suggest non-magnetic phase transitions emerge at around 110 K, likely associated with structural distortions. In sharp contrast with the first-principles calculations based on the crystal structure at room temperature, quantum oscillations reveal small Fermi pockets with light effective masses, suggesting significant change in the Fermi surface topology caused by the low temperature structural distortion. No superconductivity emerges in SrAg_4As_2 down to 2 K under pressures up to 2.13 GPa; instead, the low temperature structural distortion moves up linearly to high temperature at a rate of ≈ 13 K/GPa above 0.89 GPa.

I. INTRODUCTION

Quasi-low-dimensional materials have attracted immense research interest because they often host exotic ground states due to strong quantum and thermal fluctuations. Layered pnictide materials have provided a rich platform to explore these ground states and the competitions among them. For example, the Fermi surface nesting leads to electronic/magnetic instabilities, resulting in spin-density-wave (SDW) state in Fe pnictide superconductors [1, 2] and the charge-density-wave (CDW) in RAgSb_2 family [3, 4]. For the former, the SDW order competes with the superconductivity and quantum critical behavior was argued in P doped BaFe_2As_2 family [5]. For the latter, the CDW opens a gap at the Dirac point, leading to the exotic properties [6]. Among the layered pnictide, the ones containing AgAs have shown rich structural varieties, such as BaAg_2As_2 [7] as well the derivatives of the HfCuSi_2 structure [8]. In this paper we focus on the layered ternary pnictide SrAg_4As_2 , which crystalizes in the centrosymmetric trigonal space group $R\bar{3}m$ [9], as shown in the right inset of Fig. 1(a). It can be taken as ordered SrAg_2As_2 mixed with itinerant Ag layers, where Ag atoms (light blue balls) in the itinerant Ag layers partially occupy three different sites. As a charge-balanced Zintl phase, first-principles calculations suggest that it is a gapless system [9]. We have performed a systematic study of SrAg_4As_2 through transport and thermodynamic measurements. We show that at least one non-magnetic phase transition exists in this material and affects the electronic states in the system and results in various anomalies across the tran-

sition in its physical properties. In sharp contrast with the first-principle calculations which was performed on the room-temperature crystal structure, by examining the quantum oscillations in this material, we reveal a few much smaller Fermi pockets with light masses, pointing to the change of Fermi surface topology caused by the low temperature structural distortion.

II. SINGLE CRYSTAL GROWTH AND EXPERIMENTAL METHODS

The single crystals of SrAg_4As_2 were grown via the self-flux method. The starting materials Sr and AgAs were mixed according to the molar ratio Sr : AgAs = 1 : 4. They were loaded into a 2-ml alumina crucible and sealed inside an evacuated quartz tube. The growth ampoule was heated to 1100 °C and slowly cooled to 650 °C at a rate of 5 °C/h, at which temperature the single crystals were separated by decanting the flux in a centrifuge. Sizable plate-like single crystals were harvested, as shown in the left inset of Fig. 1(a). The typical size of the crystals can be up to $3 \times 3 \times 0.5$ mm³ and the as-grown surface is the *ab* plane.

Electrical resistivity, Hall coefficient and heat capacity data up to 300 K were collected using a Quantum Design Physical Property Measurement System (QD PPMS Dynacool). Seebeck coefficient was measured by a homemade probe inserted in the PPMS sample chamber [10]. The resistivity above 300 K was measured using a homemade probe in a tube furnace, where the tube chamber was connected to a vacuum pump to keep the pressure inside below 20 mTorr. The standard four-probe configuration was used in the electrical resistivity (ρ_{xx}) and Hall resistivity (ρ_{yx}) measurements. Four Pt wires were attached to the resistivity bar using Dupont silver paste

* Corresponding author: nini@physics.ucla.edu

7713. During the transport measurements, the magnetic field was swept from -9 T to 9 T. The data were then processed to get ρ_{xx} using $\rho_{xx}(B) = (\rho_{xx}(B) + \rho_{xx}(-B))/2$ and ρ_{yx} using $\rho_{yx}(B) = (\rho_{yx}(B) - \rho_{yx}(-B))/2$. The susceptibility was measured with a QD Magnetic Properties Measurement System (QD MPMS). The high field ρ_{xx} data up to 35 T were collected in high field magnet laboratory (HFML) in Nijmegen.

Hydrostatic pressures up to ≈ 2.13 GPa were applied using a Be-Cu piston pressure cell made by C&T Factory Co. Silicone oil (viscosity 5 cSt (25°C), Sigma-Aldrich) was used as the pressure medium. The hydrostaticity of silicone oil of a wide range of viscosities has been studied and was found to be an excellent pressure medium even up to extremely high pressures [11, 12]. The feedthrough was sealed using Stycast 2850 FT. We determined the pressure inside the sample space through the pressure dependence of the superconducting transition of Pb.

First-principles calculations based on density functional theory (DFT) were carried out to study the electronic structure. The full-potential linearized augmented plane-wave method and the generalized gradient approximation of the exchange-correlation potential as implemented in the Wien2k package were used [13].

III. EXPERIMENTAL RESULTS AND DISCUSSION

A. Physical properties of SrAg₄As₂

The temperature dependent resistivity, heat capacity, susceptibility of SrAg₄As₂ up to 300 K are presented in Fig. 1(a) and (b). It is a diamagnetic metal with ρ_0 around $3\mu\Omega\text{-cm}$. Upon cooling, between $T_1 \sim 102$ K and $T_2 \sim 117$ K, besides subsequent slope changes in resistivity as shown in Fig. 1(a) and subsequent slope changes in susceptibility as shown in the inset of Fig. 1(b), two broad peaks in heat capacity (Fig. 1(a)), which are distinct from the heat capacity with a first-order phase transition [14], are observed, featuring second order phase transitions. The Debye temperature inferred from the low temperature heat capacity is 140 K. The diamagnetic susceptibility is mainly due to the core diamagnetism of the heavy silver atoms and Landau diamagnetism, suggesting that the phase transitions lack a magnetic nature. Hereafter, we will call these transitions as the low temperature phase transitions. The left inset of Fig. 1(a) shows the temperature dependent resistivity data up to 750 K. Upon warming, besides the slope changes between 102 K and 117 K, an additional resistivity slope change was observed at $T_h \sim 715$ K, suggesting an additional high temperature non-magnetic phase transition in this compound.

The temperature dependent Hall resistivity ρ_{yx} and MR taken at 9 T are shown in Fig. 1(c). While the non-linear field dependence of ρ_{yx} shown in the inset of Fig. 1(c) suggests multi-band transport, the positive sign of

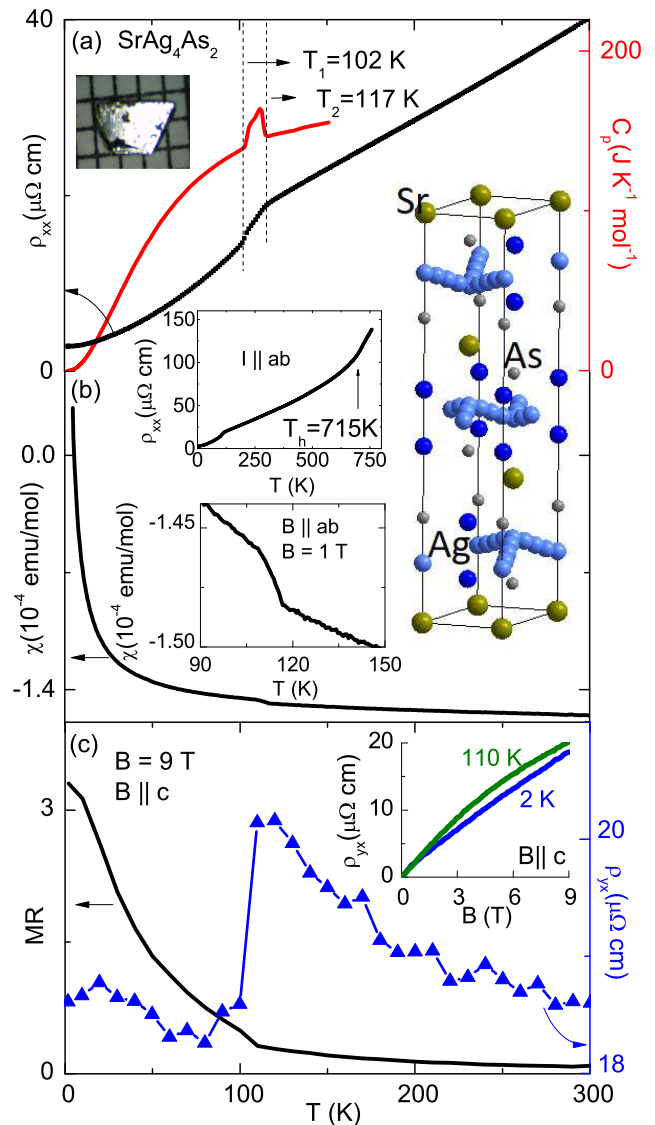


Figure 1. (a): The temperature dependent resistivity and heat capacity. Left inset: A single crystal of SrAg₄As₂ against a 1-mm scale. Top left inset: The temperature dependent resistivity measured up to 750 K. (b): The temperature dependent resistivity measured with $B \parallel ab$ at $B = 1$ T. Bottom left inset: The zoomed-in susceptibility around 110 K. Right inset: The crystal structure of SrAg₄As₂ at 300 K. Dark green ball: Sr; Dark blue ball: fully occupied Ag sites; Light blue ball: partially occupied Ag sites; Grey ball: As. (c): The temperature dependent Hall resistivity (ρ_{yx}) and transverse magnetoresistance (MR) taken at $B = 9$ T and $B \parallel c$. Inset: The field dependent ρ_{yx} taken with $B \parallel c$ at $T = 2$ K and 110 K.

ρ_{yx} suggests that holes dominate the transport. Anomalies appear in both $\rho_{yx}(T)$ and $MR(T)$. Upon cooling, ρ_{yx} first slightly increases by 8% from 300 K to the transition temperature, where it exhibits a sudden drop back to the room-temperature value; it then roughly remains constant at lower temperatures. In contrast to the roughly

temperature independent ρ_{yx} , upon cooling, the magnitude of the MR first increases by 50% across the transition; then it monotonically grows by 7 times down to 2 K. A sharp increase of the MR in the low temperature region was observed in various nonmagnetic multiband systems, such as the type-II Weyl semimetal WTe₂, the weak topological insulator NbAs₂, the Weyl semimetal TaAs, etc. [15–18], where the compensation of holes and electrons can induce the resistivity upturn (so called turn-on effect) at low temperatures [19]. For SrAg₄As₂, the 50% increase in MR likely arises due to the phase transition while the further growth of the MR at lower temperatures may originate from the turn-on effect.

Non-magnetic phase transitions can be electron-driven or lattice-driven. Electron-driven Mott phase transition is unlikely here since strong Coulomb interaction is unexpected for Ag¹⁺ ions. Lattice-driven structural phase transition is a probable candidate. Meanwhile, considering that Fermi surface nesting may show up in materials with layered structure, electron-driven charge density wave (CDW) formation is a possible candidate too. The chance of hosting a CDW transition may not be high since the resistivity anomaly in SrAg₄As₂ does not show the hump feature of a typical CDW phase transition. However, because the CDW may only gap a small portion of the Fermi surface and the formation of CDW can significantly increase the scattering rate, we still can not exclude the possibility. Further investigation using scanning tunneling microscope is needed to check if electron density modulation exists so that the two scenarios can be distinguished. Nevertheless, in both cases, structural distortions will take place. Therefore, hereafter, we will call the transitions around 110 K as low temperature structural distortions.

B. Magnetotransport properties of SrAg₄As₂

Angle-dependent transverse MR (AMR) measured with the field B perpendicular to the current is a powerful tool to probe the Fermi surface topology since the AMR is sensitive to the mobility tensor $\hat{\mu} = \tau\hat{m}^{-1}$, where τ is the relaxation time and \hat{m} is the mass tensor closely related to the Fermi surface topology [20]. Figures 2(a) and (b) show the AMR taken at 9 T at various temperatures with B rotating in the planes perpendicular to the c axis and a axis, respectively. The AMR in Fig. 2(a) with $B \perp c$ shows the threefold angular oscillations with very little anisotropy at all temperatures, consistent with the threefold rotational symmetry of the ab plane and suggesting small in-plane anisotropy. In sharp contrast, the AMR in Fig. 2(b) with $B \perp a$ shows a twofold rotational symmetry, where strong anisotropy with a ratio between the maxima and minima of about 3.5 exists, suggesting a quasi-two-dimensional electronic structure in this compound. The AMR reaches its minimum value when $B \parallel ab$ plane (0°) and gradually increases when the field rotates toward the c axis (90°) with the maxima somewhere

around 45° . This morphology suggests a more complex Fermi surface than a simple two-dimensional one. We noticed that at temperatures higher than 100 K, the feature at 45° in Fig. 2(b) is gone. It raises the question of whether the appearance of this feature is related to a significant Fermi surface reconstruction caused by the low temperature structural distortion. To clarify this, we measured AMR at 2 K with $B \perp a$ under various fields, as shown in Fig. 2(c). The solid line is the simulated curve based on a cylindrical Fermi surface assumption. At lower field, the AMR agrees well with the simulated curve and the maximum AMR appears at $B \parallel c$. With increasing field, deviations appear and the direction where the maximum AMR occurs move further and further away from the c axis. Therefore, the deviation from the two-dimensional Fermi surface observed in Figures 2(b)-(c) is more likely to be due to the fact that the mobility tensor of carriers associated with each Fermi pocket have different temperature and field dependencies.

Figure 2(d) shows the temperature dependent geometric mean of the mobilities $\bar{\mu}$ while the inset shows the field dependent electrical conductivity σ_{xy} at 2 K which was calculated using $\sigma_{xy} = \rho_{yx}/(\rho_{xx}^2 + \rho_{yx}^2)$. According to the standard Bloch-Boltzmann transport theory [21], we inferred the geometric mean of the mobilities $\bar{\mu} \equiv \sqrt{\mu_1\mu_2}$ using the formula $\bar{\mu}=1/B_{max}$, where B_{max} is the field at which $\sigma_{xy}(B)$ peaks at. $\bar{\mu}$ increases with decreasing temperature with the value of $0.5 \text{ m}^2\text{V}^{-1}\text{s}^{-1}$ at 2 K. This value is larger than that in the nodal line semimetal candidate CaAgAs [22] but smaller than those in WTe₂, Cd₃As₂, etc. [15, 21].

Figure 2(e) shows the field dependent MR up to 9 T with the current along the a axis. With $B \parallel a$, MR shows convex behavior with field. Instead of the quadratic field dependence, MR is roughly proportional to $B^{1.2}$ (the bottom inset of Fig. 2(e)). With $B \parallel c$, MR shows concave behavior with field, which may be a trend of saturation. However, even with fields up to 35 T along the c axis, no saturation is realized up to 25 K, the highest temperature we measured. MR is roughly proportional to $B^{0.75}$ in an extended field range from 2 T to 35 T and reaches 600% at 0.35 K (the top inset of Fig. 2(e)). This field dependence holds from 3 T to 35 T at 25 K. Non-quadratic field dependence of MR is non-trivial and has been observed in many materials such as the Dirac semimetal Cd₃As₂, the Weyl semimetal TaAs etc. [17, 18, 21]. The origin of this non-quadratic field dependence can arise from distinct mechanisms. Magnetism can be excluded since SrAg₄As₂ is nonmagnetic [9]. In the classical region, an open Fermi surface can lead to linear MR and a saturating Hall coefficient. This is not the case here either [23]. In the quantum limit, MR will be linear when only the lowest Landau band participates in the conductivity [24, 25]. However, the non-quadratic response in SrAg₄As₂ appears at very low field region which is away from the quantum region. Disordered systems with high mobilities, such as Ag₂Se, Dirac semimetal Cd₃As₂ and few-layer black phosphorus [21, 26–28] also show linear

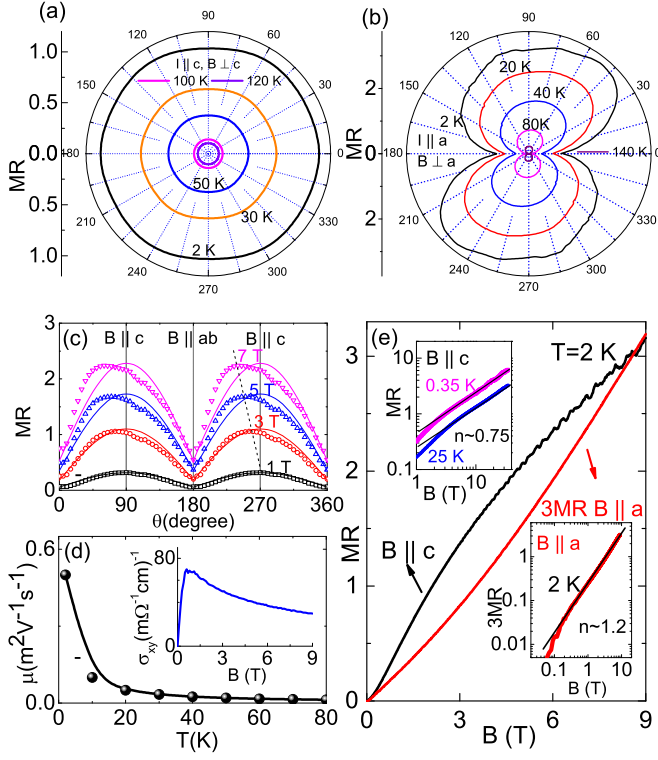


Figure 2. (a)-(b): The polar plot of the transverse angle-dependent magnetoresistance (AMR) of SrAg_4As_2 at various temperatures with $B \perp c$ and $B \perp a$ at 9 T, respectively. B is perpendicular to the current flow. (c) The AMR of SrAg_4As_2 at various fields at 2 K. Hollow symbols: Experimental data. Solid lines: Simulated AMR assuming cylindrical Fermi pocket. (d): The temperature dependent average mobility. Inset: The field dependent electrical conductivity σ_{xy} at 2 K. (e) The field dependent MR (MR(B)) at 2 K with $B \parallel c$ or $\parallel a$ up to 9 T. Top inset: The log-log plot of the MR(B) at 2 K with $B \parallel c$ up to 35 T. Bottom inset: The log-log plot of the MR(B) at 2 K with $B \parallel a$.

MR. This has been investigated using the classical disorder model [27], where Monte Carlo simulation shows that the linear MR in disordered materials with high mobility can come from the spatial fluctuation of local current density. As we will show later, indeed, the charge carriers in SrAg_4As_2 have high mobilities and small effective masses. Therefore, the linear MR in SrAg_4As_2 may suggest that local current density fluctuation plays a key role here.

C. Quantum oscillation of SrAg_4As_2

Quantum oscillations are observed in both resistivity and magnetization measurements above 1 T at low temperatures, as shown in Fig. 3(a). To shed light on the Fermi surface topology in the low temperature structure, we performed a systematic study of Shubnikov-de Haas (SdH) quantum oscillations (QO) and de Haas-van

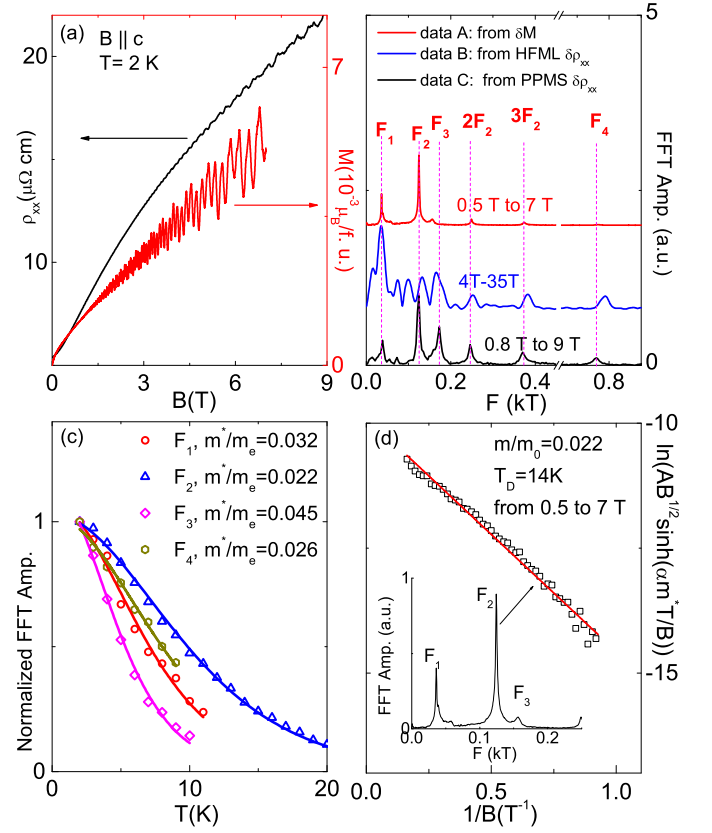


Figure 3. (a): The field dependent resistivity and magnetization at 2 K with $B \parallel c$. (b): The FFT spectra obtained from δM (data A), HFML $\delta\rho_{xx}$ (data B) and PPMS $\delta\rho_{xx}$ (data C). The FFT was performed on δM (data A) from 0.5 T to 7 T, HFML $\delta\rho_{xx}$ (data B) from 4 T to 35 T and PPMS $\delta\rho_{xx}$ (data C) from 0.8 T to 9 T, respectively. The fundamental oscillation peaks and the harmonic peaks are labeled as $F_1, F_2, 2F_2, 3F_2, F_3$ and F_4 . (c): The normalized temperature dependent FFT amplitudes of F_1, F_2, F_3 and F_4 . The FFT was performed on PPMS $\delta\rho_{xx}$ (data C) from 0.8 T to 9 T. Fits by Lifshits-Kosevich formula are denoted by solid lines. (d): The Dingle plot for F_2 obtained from δM at 2 K. Inset: The FFT spectrum of δM (data A) from 0.5 T to 7 T at 2 K.

Alphen (dHvA) QO for SrAg_4As_2 . According to the Onsager relation, the area S of the extreme cross section of the Fermi surface which is perpendicular to the applied field are related to the oscillation frequency f by the equation $f = \frac{\hbar}{2\pi} S$ [29]. Figure 3(b) presents the Fast Fourier transformation (FFT) spectra of the oscillating $\delta\rho_{xx}$ and δM , where $\delta\rho_{xx}$ and δM are obtained by subtracting a polynomial background from ρ_{xx} and M , respectively. Different oscillation frequencies are detected. Combining all three sets of data measured on different samples [30], we were able to assign the oscillations to four fundamental frequencies ($F_1 = 38$ T, $F_2 = 125$ T, $F_3 = 173$ T, $F_4 = 760$ T) and the harmonics of F_2 , as labeled in Fig. 3(b). The amplitude of the oscillations

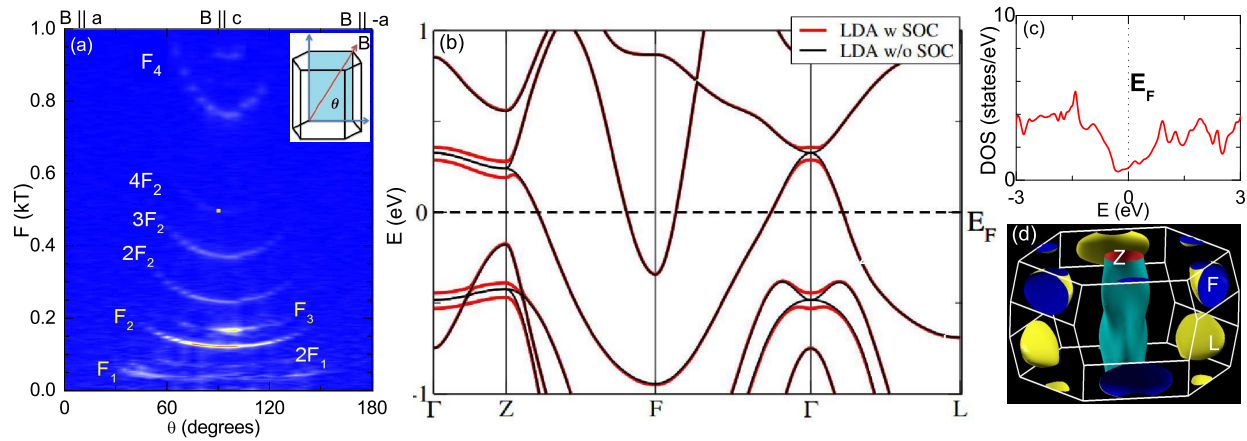


Figure 4. (a): The color plot of angle-dependent FFT of $\delta\rho_{xx}$ with the rotation geometry shown in the inset. (b): The band structure calculated from first-principles calculations with density-functional theory (DFT) using the crystal structure at 300 K. (c): The density of states based on the DFT calculation. (d): The Fermi surface based on the DFT calculation using the crystal structure at 300 K.

Table I. The frequency and effective mass of the fundamental frequencies. The data analysis was made on the FFT of data C and data A, respectively.

	FFT window	F ₁	F ₂	F ₃	F ₄
Frequency(T)	0.8 T - 9 T	38	124	173	760
m/m ₀ (data C)	0.8 T - 9 T	0.032	0.022	0.045	0.026
m/m ₀ (data C)	1.6 T - 9 T	0.058	0.043	0.081	0.049
m/m ₀ (data C)	3.2 T - 9 T	0.081	0.060	0.12	0.078
m/m ₀ (data A)	0.5 T - 7 T	0.028	0.022	-	-
T _D (data A)	0.5 T - 7 T	-	14 K	-	-

can be described by the Lifshits-Kosevich formula [29]

$$A(B, T) \propto \frac{\alpha T m^*/B}{\sinh(\alpha T m^*/B)} \exp(-\alpha T_D m^*/B) \quad (1)$$

where $\alpha = 2\pi^2 k_B m_e / e\hbar = 14.69$ T/K, m^* is the cyclotron effective mass and $T_D = \frac{\hbar}{2\pi k_B \tau_s}$ is the Dingle temperature which is a measure of the single-particle scattering rate τ_s . Figure 3(c) shows the temperature dependencies of the normalized amplitude of FFT for the four fundamental frequencies using data C. By performing FFT on data C at various temperatures in FFT window with the interval of fields B_1 and B_2 , we can fit the $A(B, T)$ of each fundamental FFT peak using the Equ. (1) with $1/B = (1/B_1 + 1/B_2)/2$ (see Fig. 3(c)). The obtained effective masses using different FFT window are summarized in table I, being quite small compared to those in LaSb and LaBi [31, 32]. The inset of Fig. 3(d) shows the zoomed-in plot of FFT spectrum of δM using data A at 2 K. The F_2 peak can be easily separated from F_1 and F_3 peaks and a Dingle plot can be obtained as shown in Fig. 3(d)[16]. By fitting the data, $T_D = 14$ K is inferred and the τ_s is estimated to be 8.7×10^{-14} s.

To further investigate the Fermi surface topology, we

studied the angle-dependent SdH oscillations and compared them with the first-principles calculations. The measurement geometry is shown in the inset of Fig. 4(a). B was rotated from the a axis to the c axis and then to the $-a$ axis. The angle-dependent FFT spectra of $\delta\rho_{xx}$ obtained using data C are presented in Fig. 4(a). Both F_2 and F_3 have minima at $B \parallel c$ and increase with the field B rotating away from the c axis, suggesting that the associated Fermi pockets have the minimum extreme cross sections in the plane perpendicular to c .

To understand the observed SdH, DFT band structure calculations were performed using the crystal structure in Ref. [9] obtained at 300 K. The referenced crystal structure shows that there are four Ag sites. Two of them have very low occupancies (0.051(3) and 0.036(4)), one has a higher occupancy of 0.789(8) and another is set to be fully occupied. To simplify the calculation, the Ag sites with low partial occupancies are ignored while the Ag site with larger partial occupancy is fully occupied. Figure 4(c) shows the density of states (DOS) plot. It suggests a semimetallic character for SrAg₄As₂, consistent with experiments. The DOS at the Fermi level is dominated by arsenic p orbitals while the Ag d orbital weights small. Therefore, although our DFT calculation employed simplified crystal structure ignoring the Ag sites with low occupancies, it should keep the main features of the Fermi surface. Figure 4(b) shows the DFT band structure. The feature of the band structure near the Fermi level is not affected by spin-orbit coupling. Two types of Fermi pockets exist, as shown in Fig. 4(d). The hole pocket centered at the Γ point is two dimensional along the Γ -Z direction with the effective mass of $0.4m_e$ when $B \parallel c$ while the electron pocket centered at the F point is a three dimensional oblate ellipsoid with the effective mass of $0.5m_e$ when $B \parallel c$, consistent with the electron-hole compensation suggested by the observed turn-on effect. However, the inferred frequencies from the minimum extreme cross

section of the two Fermi pockets are around 1000 T, much larger than F_1 to F_3 (7 T, 125 T and 173 T) we observed experimentally but reasonably close to the $F_4 \sim 780$ T.

Considering the small SdH Fermi pockets with extremely small effective masses and the dramatic discrepancy between QO and DFT calculations, the Fermi surface topology must have changed significantly due to the low temperature structural distortion. Unexpected small Fermi pockets have been discovered in Cuprates, as the result of the band folding effect due to the formation of CDW [33, 34] while banding folding has been observed in Fe-based superconductors due to the structural and magnetic phase transitions [35]. At low temperatures, the structural modulation expands the unit cell and lowers the symmetry of the crystal. As a consequence, the Brillouin zone is folded and small Fermi pockets can appear. Further investigation is needed to clarify the origin of this low temperature structural distortion and thus to explain if the small Fermi pockets observed are from a simple band folding effect.

D. The effect of external pressure on SrAg_2As_2

Tuning the phase transitions using either chemical doping/intercalation or external pressure may result in unusual ground states. For example, suppressing the CDW order in TiSe_2 using Cu intercalation has led to the appearance of superconductivity [36]. The suppression of SDW in LaFeAsO by F doping on the O sites has made the discovery of the second high temperature superconducting family [2]. To tune the ground state of SrAg_4As_2 , we applied external hydrostatic pressure on a piece of SrAg_4As_2 with a RRR of ≈ 18 at ambient pressure. Figure 5(a) shows the evolution of $\rho(T)$ under the application of external pressure up to 2.13 GPa. No superconductivity is observed. Figure 5(b) shows the first derivative of the $\rho(T)$ at various pressures. Below 0.89 GPa, the transition temperature is slightly suppressed with pressure at a rate of 3.2 K/GPa and then starts to increase linearly at a rate of ≈ 13 K/GPa up to 2.13 GPa, the highest pressure we applied. The T-P phase diagram is summarized in Fig. 5(c) where the non-magnetic transition temperature T_s is determined by the criterion shown in Fig. 5(b). The T-P phase diagram shows a v-shaped pressure dependence of the transition temperature. The drop in resistivity across the transition, $\Delta\rho_{xx}$, was determined using the criterion shown in the inset of Fig. 5(a). $\Delta\rho_{xx}$ first decreases and then increases with pressure, in a similar manner as T_s , as shown in Fig. 5(c). Both pressure dependent transition temperature and $\Delta\rho_{xx}$ that we observe here are reminiscent of the evolution of the CDW transition in SmNiC_2 under pressure [37, 38].

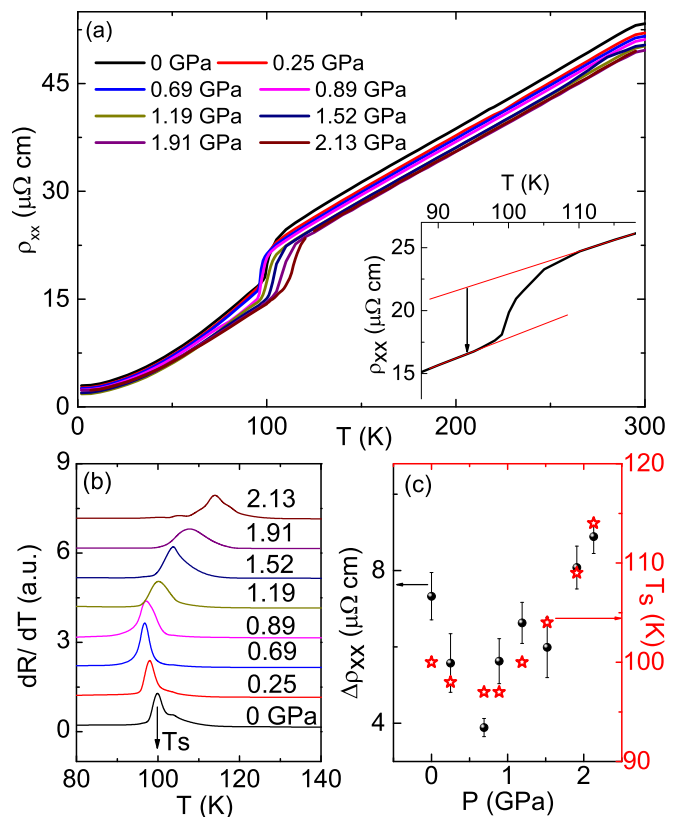


Figure 5. (a): The temperature dependent resistivity of SrAg_4As_2 under various pressure. Inset: The criterion to determine the $\Delta\rho_{xx}$. (b) The dR/dT at various pressure. The criterion to determine T_s is shown. (c) The temperature-pressure (T-P) phase diagram and the drop in resistivity $\Delta\rho_{xx}$ across the transition as a function of pressure. The error bars correspond to the standard deviation of an average of six calculations.

IV. CONCLUSION

In conclusion, SrAg_2As_2 shows electronic changes across the low temperature structural distortion around 110 K, which manifest in clear anomalies in the temperature dependent electrical and Hall resistivity, heat capacity, susceptibility and magnetoresistance (MR). In addition, a high temperature structural distortion around 715 K was evidenced by a slope change in resistivity. Angle-dependent MR measurements show small in-plane anisotropy but large out-of-plane anisotropy, suggesting a two-dimensional electronic structure. Multi-band transport is observed; large non-saturating MR was observed with high mobility, consistent with the semimetallic nature revealed by the DFT calculation. MR shows non-trivial field dependence, which may be due to charge fluctuation in this highly disordered material. Both dHvA and SDH oscillation reveal small Fermi pockets with light effective masses, while the DFT calculation based on the room temperature crystal structure leads to Fermi pockets with much larger size and heavier masses. We at-

tribute this discrepancy to the significant change in the Fermi surface topology caused by the low temperature structural distortion. The application of external hydrostatic pressure first suppresses the transition below 0.89 GPa and then enhances the phase transition linearly at a rate of ≈ 13 K/GPa up to 2.13 GPa without inducing superconductivity.

ACKNOWLEDGMENTS

Work at UCLA was supported by the U.S. Department of Energy (DOE), Office of Science, Office of Basic Energy Sciences under Award Number DE-SC0011978. AIC acknowledges an EPSRC Career Acceleration Fellowship (EP/I004475/1). Part of this work was supported by HFML-RU/FOM and LNCMI-CNRS, members of the European Magnetic Field Laboratory (EMFL) and by EPSRC (UK) via its membership to the EMFL (grant no. EP/N01085X/1). Work at Rutgers was supported by the NSF DMREF program under the award NSF DMREF project DMR-1435918. NN would like to thank useful discussion with Gui Xin and Prof. Weiwei Xie.

-
- [1] J. Dong, H. J. Zhang, G. Xu, Z. Li, G. Li, W. Z. Hu, D. Wu, G.F. Chen, X. Dai, J. L. Luo, Z. Fang and N. Wang, *Europhys. Lett.* **83**, 27006 (2008).
- [2] C. de la Cruz, Q. Huang, J. W. Lynn, J. Li, W. Ratcliff II, J. L. Zarestky, H. A. Mook, G. F. Chen, J. L. Luo, N. L. Wang and P. Dai, *Nature* **453**, 899 (2008).
- [3] C. Song, J. Park, J. Koo, K.-B. Lee, J. Y. Rhee, S. L. Budko, P. C. Canfield, B. N. Harmon and A. I. Goldman, *Phys. Rev. B* **68**, 035113 (2003)
- [4] S. L. Budko, T. A. Wiener, R. A. Ribeiro, P. C. Canfield, Y. Lee, T. Vogt, and A. H. Lacerda, *Phys. Rev. B* **73**, 184111 (2006)
- [5] Q. Si, R. Yu and E. Abrahams, *Nat. Rev. Mater.* **1**, 16017 (2016).
- [6] X. Shi, P. Richard, K. Wang, M. Liu, C. E. Matt, N. Xu, R. S. Dhaka, Z. Ristic, T. Qian, Y.-F. Yang, C. Petrovic, M. Shi, and H. Ding, *Phys. Rev. B* **93**, 081105(R) (2016).
- [7] S. S. Stoyko, P. E.R. Blanchard, A. Mar, *J. Solid State Chem.* **194**, 113 (2012)
- [8] R. Demchyna, J. P. F. Jemetio, Yu. Prots, Th. Doert, L. G. Akselrud, W. Schnelle, Yu Kuzma, and Yu Grin, *Z. anorg. allg. Chem.* **630**, 635 (2004)
- [9] S. S. Stoyko, M. Khatun, C. S. Mullen and A. Mar, *J. Solid State Chem.*, **192** 325, (2012).
- [10] Eundeok Mun, Sergey L Bud'ko, Milton S Torikachvili and Paul C Canfield, *Meas. Sci. Technol.*, **21**, 055104 (2010)
- [11] Y. Shen, R.S. Kumar, M. Pravica, and M.F. Nicol, *Rev. Sci. Instrum.* **75**, 4450 (2004)
- [12] D.D. Ragan, D.R. Clarke, and D. Schiferl, *Rev. Sci. Instrum.* **67**, 494 (1996)
- [13] P. Blaha, K. Schwarz, G. Madsen, D. Kvasnicka, and J. Luitz, *wien2k, An augmented Plane Wave + Local Orbitals Program for Calculating Crystal Properties* (Techn. Universitat Wien, Austria, 2001).
- [14] N. Ni, S. Nandi, A. Kreyssig, A. I. Goldman, E. D. Mun, Sergey L Bud'ko, and P. C. Canfield, *Phys. Rev. B* **78**, 014523 (2016)
- [15] M. N. Ali, J. Xiong, S. Flynn, J. Tao, Q. D. Gibson, L. M. Schoop, T. Liang, N. Haldolaarachchige, M. Hirschberger, N. P. Ong and R. J. Cava, *Nature* **514**, 205 (2014).
- [16] B. Shen, X. Deng, G. Kotliar, and N. Ni, *Phys. Rev. B* **93**, 195119 (2016).
- [17] X. Huang, L. Zhao, Y. Long, P. Wang, D. Chen, Z. Yang, H. Liang, M. Xue, H. Weng, Z. Fang, X. Dai, and G. Chen, *Phys. Rev. X* **5**, 031023 (2015).
- [18] C. Zhang, S.-Y. Xu, I. Belopolski, Z. Yuan, Z. Lin, B. Tong, N. Alidoust, C.-C. Lee, S.-M. Huang, H. Lin, M. Neupane, D. S. Sanchez, H. Zheng, G. Bian, J. Wang, C. Zhang, T. Neupert, M. Z. Hasan, and S. Jia, *Nat. Commun.* **7**, 10735 (2016).
- [19] Y. L. Wang, L. R. Thoutam, Z. L. Xiao, J. Hu, S. Das, Z. Q. Mao, J. Wei, R. Divan, A. Luican-Mayer, G. W. Crabtree, and W. K. Kwok, *Phys. Rev. B* **92**, 180402(R)
- [20] A. Collaudin, B. Fauque, Y. FUSEYA, W. Kang, K. Behnia, *Phys. Rev. X* **5**, 021022, 2015.
- [21] T. Liang, Q. Gibson, M.N. Ali, M. Liu, R.J. Cava, and N.P. Ong, *Nat. Mater.* **14**, 280 (2015).
- [22] E. Emmanouilidou, B. Shen, X. Deng, T.-R. Chang, A. Shi, G. Kotliar, S.-Y. Xu, and N. Ni, *Phys. Rev. B* **95**, 245113 (2017).
- [23] A. B. Pippard, *Magnetoresistance in Metals* (Cambridge University Press, 1984).
- [24] A. A. Burkov, M. D. Hook, and L. Balents, *Phys. Rev. B* **84**, 235126 (2011).
- [25] P. Goswami, J. H. Pixley, and S. Das Sarma, *Phys. Rev. B* **92**, 075205 (2015).
- [26] M. M. Parish and P. B. Littlewood, *Nature* **426** 162, (2003).
- [27] A. Narayanan, M. D. Watson, S. F. Blake, N. Bruyant, L. Drigo, Y. L. Chen, D. Prabhakaran, B. Yan, C. Felser, T. Kong, P. C. Canfield, and A. I. Coldea, *Phys. Rev. Lett.* **114**, 117201 (2015).
- [28] Z. Luo, J. Maassen, Y. Deng, Y. Du, R. P. Garrelts, M. S. Lundstrom, P. D. Ye and X. Xu, *Nat. Commun.* **6**, 8572 (2014).
- [29] D. Shoenberg, *Magnetic Oscillations in Metals* (Cambridge University Press, Cambridge, 1984).
- [30] See supplemental information.
- [31] F. F. Tafti, Q. D. Gibson, S. K. Kushwaha, N. Haldolaarachchige and R. J. Cava, *Nature Physics* **12**, 272 (2016).
- [32] S. Sun, Q. Wang, P.-J. Guo, K. Liu, and H. Lei, *New J. Phys.* **18**, 082002 (2016).
- [33] Nicolas Doiron-Leyraud, Cyril Proust, David LeBoeuf, Julien Levallois, Jean-Baptiste Bonnemaïson, Ruixing Liang, D. A. Bonn, W. N. Hardy and Louis Taillefer,

- Nature 447, 565 (2007).
- [34] J. Chang, E. Blackburn, A. T. Holmes, N. B. Christensen, J. Larsen, J. Mesot, Ruixing Liang, D. A. Bonn, W. N. Hardy, A. Watenphul, M. v. Zimmermann, E. M. Forgan and S. M. Hayden, Nat. Phys. 8, 871(2012).
- [35] James G. Analytis, Ross D. McDonald, Jiun-Haw Chu, Scott C. Riggs, Alimamy F. Bangura, Chris Kucharczyk, Michelle Johannes, and I. R. Fisher, Phys. Rev. B 80, 064507 (2009)
- [36] E. Morosan, H. W. Zandbergen, B. S. Dennis, J. W. G. Bos, Y. Onose, T. Klimczuk, A. P. Ramirez, N. P. Ong and R. J. Cava, Nat. Phys. **2**, 544 (2006).
- [37] J.N.Kim, C.Lee and J.-H. Shim, New J. Phys. **15**, 123018 (2013).
- [38] B. Woo, S. Seo, E. Park, J.H. Kim, D. Jang, T. Park, H. Lee, F. Ronning, J.D. Thompson, V.A. Sidorov, and Y.S. Kwon, Phys. Rev. B **87**, 125121 (2013).